Seasonal and Interannual Variations of Irminger Ring Formation and Boundary–Interior Heat Exchange in FLAME

M. F. DE JONG

Duke University, Durham, North Carolina, and Royal Netherlands Institute for Sea Research (NIOZ), Texel, Netherlands

A. S. BOWER AND H. H. FUREY

Woods Hole Oceanographic Institution, Woods Hole, Massachusetts

(Manuscript received 21 July 2015, in final form 8 March 2016)

ABSTRACT

The contribution of warm-core anticyclones shed by the Irminger Current off West Greenland, known as Irminger rings, to the restratification of the upper layers of the Labrador Sea is investigated in the 1/12° Family of Linked Atlantic Models Experiment (FLAME) model. The model output, covering the 1990–2004 period, shows strong similarities to observations of the Irminger Current as well as ring observations at a mooring located offshore of the eddy formation region in 2007–09. An analysis of fluxes in the model shows that while the majority of heat exchange with the interior indeed occurs at the site of the Irminger Current instability, the contribution of the coherent Irminger rings is modest (18%). Heat is provided to the convective region mainly through noncoherent anomalies and enhanced local mixing by the rings facilitating further exchange between the boundary and interior. The time variability of the eddy kinetic energy and the boundary to interior heat flux in the model are strongly correlated to the density gradient between the dense convective region and the more buoyant boundary current. In FLAME, the density variations of the boundary current are larger than those of the convective region, thereby largely controlling changes in lateral fluxes. Synchronous long-term trends in temperature in the boundary and the interior over the 15-yr simulation suggest that the heat flux relative to the temperature of the interior is largely steady on these time scales.

1. Introduction

Deep convection in the Labrador Sea, which forms Labrador Sea Water, has been studied extensively in the field (Lazier 1980; Talley and McCartney 1982; Lab Sea Group 1998; Lazier et al. 2002; Pickart et al. 2002; Haine et al. 2008). Historic data indicate that strong convection events, with consecutive years of deep convective mixing, occur nearly every 10 years (van Aken et al. 2011). Two large events during the modern observational period were seen in the early 1990s and early 2000s. The spreading of the two distinct Labrador Sea Water classes formed during these events into the subpolar gyre has been monitored closely (Rhein et al. 2002; Kieke et al. 2006; Yashayaev 2007; Kieke and Yashayaev 2015). Some model studies (Biastoch et al. 2008; Danabasoglu et al. 2012) suggest that Labrador Sea convection has an important role within the Atlantic meridional overturning circulation (AMOC), as the AMOC may slow down as a result of weakened deep convection. This could occur when large amounts of freshwater are released from Greenland's glaciers (Manabe and Stouffer 1995; Vellinga and Wood 2002), creating conditions similar to the Great Salinity Anomaly (Dickson et al. 1988).

While deep convection and its response to freshwater forcing have been studied in detail since the 1980s, their counterpart, restratification, has only gained attention over the last decade (Katsman et al. 2004; Straneo 2006). Several studies indicate that restratification of the

Denotes Open Access content.

Corresponding author address: M. F. de Jong, Nicholas School of the Environment, Duke University, 5117 Environment Hall, Box 90328, Durham, NC 27708-0328.
E-mail: femke.de.jong@duke.edu

DOI: 10.1175/JPO-D-15-0124.1

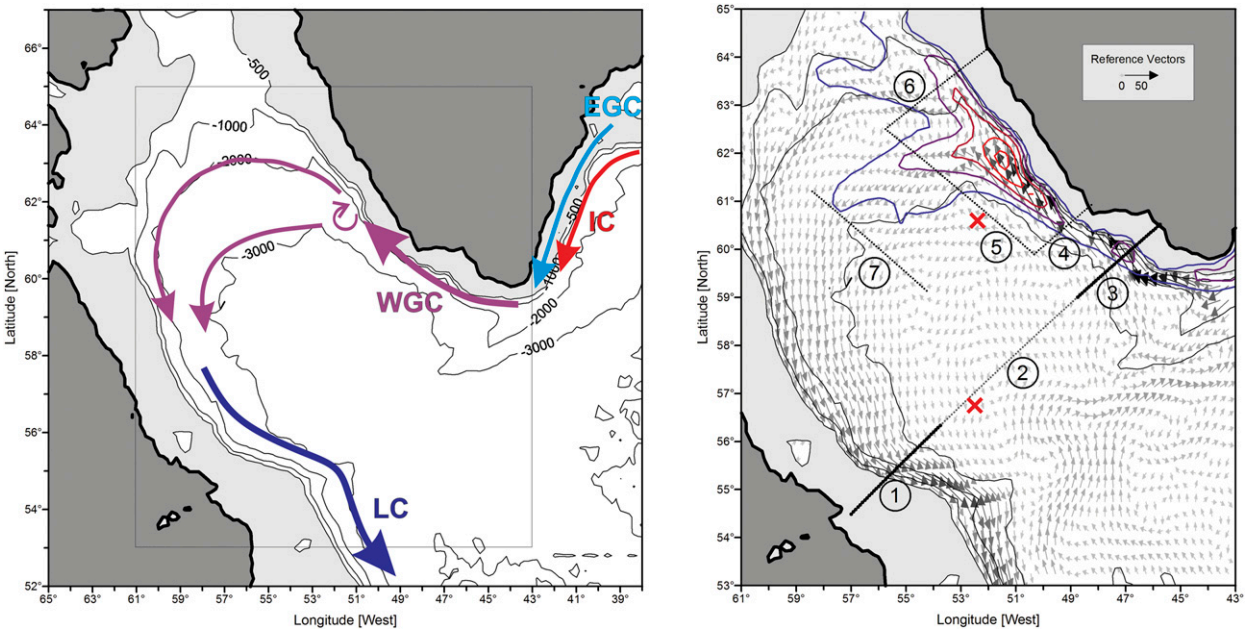

FIG. 1. (left) Map of the Labrador Sea with schematic of currents. Acronyms for the currents denote the East Greenland Current (EGC), Irminger Current (IC), West Greenland Current (WGC), and the Labrador Current (LC). The purple color of the WGC indicates the merging (or vertical stacking) of the cold EGC and the warmer IC. At the steep transition in the West Greenland continental slope the WGC becomes unstable, forms eddies, and splits into two branches. These branches merge into the LC on the western side of the basin, which has significantly cooled by now and is therefore drawn in blue. (right) Zoom-in on the Labrador Sea (area bounded by the rectangle in the left panel) showing the mean current vectors at the 516 m depth level. EKE contours are drawn starting at 250 $cm^2 s^{-2}$ (blue) and then every next 250 $cm^2 s^{-2}$ (going to red). The section across the entrance of the Labrador Sea used in the analysis is drawn as well as the box around the EKE maximum. The (sub)sections are 1) LC, 2) CENTER, 3) WGC, 4) IN, 5) FLANK, 6) OUT, and 7) MID. The location of the IRINGS mooring in indicated by the red cross off the FLANK section. The Bravo mooring is indicated by the red cross off the CENTER section. Isobaths are drawn at 500, 1000, 2000, and 3000 m.

convective region occurs at least in part through coherent rings shed by the West Greenland Current (WGC; Fig. 1; Prater 2002; Lilly and Rhines 2002; Lilly et al. 2003; Hátún et al. 2007). The WGC transports cold freshwater from the East Greenland Current in its upper layers and warm, salty water from the Irminger Current at mid-depths (Fratantoni and Pickart 2007). As the topography of the West Greenland slope steepens around 61°N, the boundary current becomes unstable (Eden and Böning 2002; Bracco and Pedlosky 2003; Wolfe and Cenedese 2006). This generates an eddy kinetic energy (EKE) maximum offshore of West Greenland (Fig. 1). The EKE reaches a maximum in January (Prater 2002; Lilly et al. 2003; Brandt et al. 2004). Some fraction of the EKE results from the shedding of coherent Irminger rings, named after their core of warm Irminger Current water. These rings, fast moving and with radii of approximately 20 km (Lilly and Rhines 2002; Hátún et al. 2007; Rykova et al. 2009), are difficult to track individually in satellite-derived altimetry observations (de Jong et al. 2014).

While the variability of Labrador Sea Water in the interior Labrador Sea is relatively well observed by the annual sections along the Atlantic Repeat Hydrography Line 7 West (AR7W; Yashayaev 2007) and Argo floats, the WGC is less well sampled. Rykova et al. (2015) described the seasonal variability of the WGC using hydrographic occupations between 1990 and 2005 combined with altimetry. They constructed summer (May–July) and winter (October–February) climatologies. The core of the Irminger Water (IW) in the WGC was found to be about 0.6°C warmer and 0.01 psu saltier in winter than in summer. Rykova et al. (2015) also showed that the current velocity varied seasonally, with largest velocities in fall when the baroclinic component is strongest. De Jong et al. (2014) found a seasonal cycle in the properties of Irminger rings observed between September 2007 and September 2009. During this period Irminger ring cores in fall were on average 1.9°C warmer and 0.07 psu saltier than in spring. De Jong et al. (2014) suggested that this seasonal cycle related directly to the seasonal cycle in the IW, with the larger range in core properties being the result of interannual variability in the IW. Myers et al. (2007) found an increasing trend in the temperature and salinity of Irminger Water since 1995. However, both the datasets used by Myers et al. (2007) and Rykova et al. (2015) originated mostly from

the summer months and did not capture the winter extremes in WGC core properties.

A large field program, Overturning in the Subpolar North Atlantic Program (OSNAP; http://www.o-snap.org), is currently underway and will sample the WGC in detail. We aim to provide a model background against which these future observations can be compared. Previous model studies of Irminger rings have shown the potential importance of these features in (re)setting the stratification of the Labrador Sea (Katsman et al. 2004; Chanut et al. 2008; Gelderloos et al. 2011). However, these models were either highly idealized in basin geometry and hydrography (Katsman et al. 2004; Gelderloos et al. 2011) or assumed an idealized forcing (Chanut et al. 2008). Recent studies with more realistic models have explored the seasonality of the EKE (Luo et al. 2011), the lateral heat transport after convection in 2008 (Zhang and Yan 2014), and the difference between resolved and parameterized eddies (Saenko et al. 2014). However, these latter studies did not investigate the role of eddies in restratification directly.

The present study aims to elucidate the transport of heat from the boundary current to the convective area in the Labrador Sea and the role that Irminger rings play therein. We will focus on the seasonal and interannual variability of the Irminger rings provided by a simulation by a realistic model forced by varying atmospheric conditions between 1990 and 2004, as these were missing from earlier idealized model studies. The model used in this study, the 1/12° Family of Linked Atlantic Models Experiment (FLAME) model, is presented in section 2 as well as the eddy detecting and tracking algorithms. In section 3 we first compare the model circulation and the identified model eddies to the available observations. We follow this by an analysis of volume, heat, and freshwater fluxes. We investigate the contributions of the coherent eddies as well as the anomaly fluxes, which will shed light on the mean sources of heat in the basin. We finish this section with a discussion of the interannual variability in the 15-yr model time series. Section 4 concludes this manuscript with a summary and discussion.

2. Model output and analysis methods

This study uses the interannual run of the FLAME model, which has been described by Eden and Böning (2002), Biastoch et al. (2008), and Gary et al. (2011). It is a 1/12° Mercator grid model with 45 vertical (z coordinate) levels, based on the Modular Ocean Model, version 2.1 (MOM2.1; Pacanowski 1996). The model is spun up from the Levitus and Boyer (1994) and Levitus et al. (1994) climatology forced with European Centre for Medium-Range Weather Forecasts (ECMWF) climatology. It is then run from 1990 to 2004 by a combination of the climatology and monthly anomalies from NCEP–NCAR reanalysis data. The 3-day snapshots of velocity, temperature, and salinity stored during the 1990–2004 period are analyzed in this study. Eden and Böning (2002) found the FLAME representation of the Labrador Sea EKE to be in reasonable agreement with the observations. Since then the model has been used for various studies of the North Atlantic (Biastoch et al. 2008; Bower et al. 2009, 2011; Gary et al. 2011; Burkholder and Lozier 2011; Lozier et al. 2013). A more thorough description of the FLAME model and how its eddy representation improved the performance of the model can be found in Czeschel (2004). These results support the use of FLAME for the present study of eddy processes in the Labrador Sea.

We used the eddy detection method described by Nencioli et al. (2010) to identify mesoscale eddies in the FLAME velocity fields for the Labrador Sea region between 60° and 45°W and 55° and 65°N. (MATLAB scripts for this method are available at http://www.com.univ-mrs.fr/~nencioli/research.php?type=eddy_detect.) This is an automated eddy detection method that uses the geometry of the velocity vectors. Unlike the Okubo–Weiss method, which relies on often noisy gradients of velocity, it does not require smoothing of the velocity fields and thus allows for detection of smaller features. The Nencioli algorithm looks for locations where four constraints are satisfied: first, a reversal of the northward velocity v along an east–west section; second, a reversal of the eastward velocity u along a north–south section with a similar sense of rotation as v; third, a local minimum of the velocity magnitude at the eddy center; and last, a constant sense of rotation along the four quadrants of the eddy. When all four conditions are satisfied, the algorithm determines the last closed streamline from the eddy center within which the radial velocity increases outward from the center. This assumes that radial velocities are maximum at radius R, similar to a Rankine eddy (Lilly and Rhines 2002). The method identifies latitude and longitude of the center of the eddy as well as the shape of the closed streamline and the type of eddy (cyclone or anticyclone). Two parameters can be set that determine the limits of detection. For this study, we chose the parameters such that they picked up the smallest eddies (two grid points). All selected eddies were then filtered, as we will discuss next.

Irminger rings have surface-intensified velocity profiles (Lilly et al. 2003; Hátún et al. 2007; de Jong et al. 2014), so we used the 5-m-depth model velocity field to detect eddies using the Nencioli algorithm. For each detected eddy, a least squares fit to an ellipse was made

on the shape of the closed streamline in order to determine the effective radius and eccentricity of the eddy. Since the effective grid scale in the central Labrador Sea in FLAME is 4.6 km, we set a minimum effective radius of 9 km for the eddy to remain in the final dataset. Since we are interested in deep-reaching Irminger rings rather than shallow features, we further filtered the detected eddies based on the 250-m model density field. Eddies had to pass a criterion on the 250-m density anomaly within the eddy. The density anomaly was determined by subtracting a 4.5-month running mean of the local density from the density within the eddy radius. The 4.5-month mean was chosen to limit the local effect of slow-moving eddies while maintaining the seasonal variability of the background. Eddies with an absolute density anomaly smaller than $0.002\,\mathrm{kg\,m^{-3}}$, or with a density anomaly sign that did not match their sense of rotation, were discarded (assuming a deep level of no motion as observed). Of all detected eddies, 11% were discarded because their radius was smaller than 9 km and 13% because their density anomaly at 250 m was too small and/or of a sign not consistent with the rotation.

The Nencioli script also provides a method of eddy tracking. For each (anti)cyclone at time step t_0, it searches for the nearest (anti)cyclone at time t_1. The nearest (anti)cyclone has to be within a given search radius of the position at t_0. In the FLAME data this resulted in predominantly short tracks (average of four time steps or 12 days). Therefore, we employed a different method here. At each time step ''virtual'' particles were deployed in the velocity field along the center line of a detected eddy. These particles were tracked backward and forward in time from the eddy position. Particle trajectories were computed using a variable-step fourth-order Runge–Kutta integration scheme with the bilinear velocity interpolation in time and space between the grid points. This scheme was used earlier by Rypina et al. (2011, 2012). Particles captured within the eddy center show cyclic tracks that remain near the eddy center, while particles that are not captured generally show smooth tracks and diverge from the eddy center. Tracks captured within the eddy were separated from diverging tracks using Lilly's wavelet method (Bower et al. 2013; script available at http://www.jmlilly.net/jmlsoft.html). The algorithm then matched (anti)cyclones along the center of the remaining particle tracks. While this method is computationally more costly than a simple search for the closest eddy, it has two distinct advantages. First, the size and direction of the search area of matching eddies is now set by the local flow field rather than by arbitrarily setting a fixed range. Second, eddy tracks need not stop when an eddy was not detected (or was filtered out by postprocessing) for a time step along the track. This reduces the ''disappearance'' and ''appearance'' of eddies along tracks. We allowed an eddy to temporarily disappear along a track for a maximum of two time steps. To be allowed back on the track after one or two missing steps, it not only had to be near the simulated particle tracks, but the eddy's density anomaly also had to be within $0.02\,\mathrm{kg\,m^{-3}}$ of the anomaly last seen on the track.

Studies using observations of eddies (Hátún et al. 2007; Rykova et al. 2009; de Jong et al. 2014) calculated heat and freshwater content of individual eddies. For comparison, similar heat content H and freshwater content F for individual eddies found using the eddy detection algorithm were calculated using

$$H = \int_0^{1.5R}\int_{z1}^{z2} \rho c_p (T - T_{\mathrm{ref}})\, dz\, dr \quad \text{and} \tag{1}$$

$$F = \int_0^{1.5R}\int_{z1}^{z2} [1 - (S/S_{\mathrm{ref}})]\, dz\, dr, \tag{2}$$

integrating vertically between two layers, 0–200 m and 200–1000 m. These two layers are used in earlier observational studies (Hátún et al. 2007; de Jong et al. 2014) and contain most of the property anomaly. Variable R is the eddy radius, $\rho = 1027\,\mathrm{kg\,m^{-3}}$ is the reference density, and $c_p = 4000\,\mathrm{J\,kg^{-1}\,C^{-1}}$ is the heat capacity of seawater. Variables T_{ref} and S_{ref} are reference values and are chosen to be the minimum temperature and salinity of the mean seasonal cycle in the convective region (3.35°C and 34.93, respectively, in this FLAME simulation). In a separate calculation, conducted to exclude the increasing trend in temperature and salinity seen in the entire basin over the record, $T_{\mathrm{ref}}(t)$ and $S_{\mathrm{ref}}(t)$ were chosen to be the time-varying mean temperature and salinity of the upper 1 km in the convective region. The horizontal integration scale, from the center out to $1.5R$, was chosen because the temperature and salinity maxima often extend outside the radius of maximum velocity (Hátún et al. 2007). Outside of $1.5R$, other nearby eddies or anomalies start to influence the derived heat content. The volume of each eddy is assumed to be the volume of integration, a cylinder $1.5R$ wide and 1000 m deep.

3. Results

a. *Comparison of the model circulation with observations*

The mean WGC in the FLAME model reasonably resembles the observed mean current (Fig. 2). The FLAME WGC also shows a strong seasonal cycle similar to the observations described by Rykova et al. (2015). The temperature and salinity of the Irminger

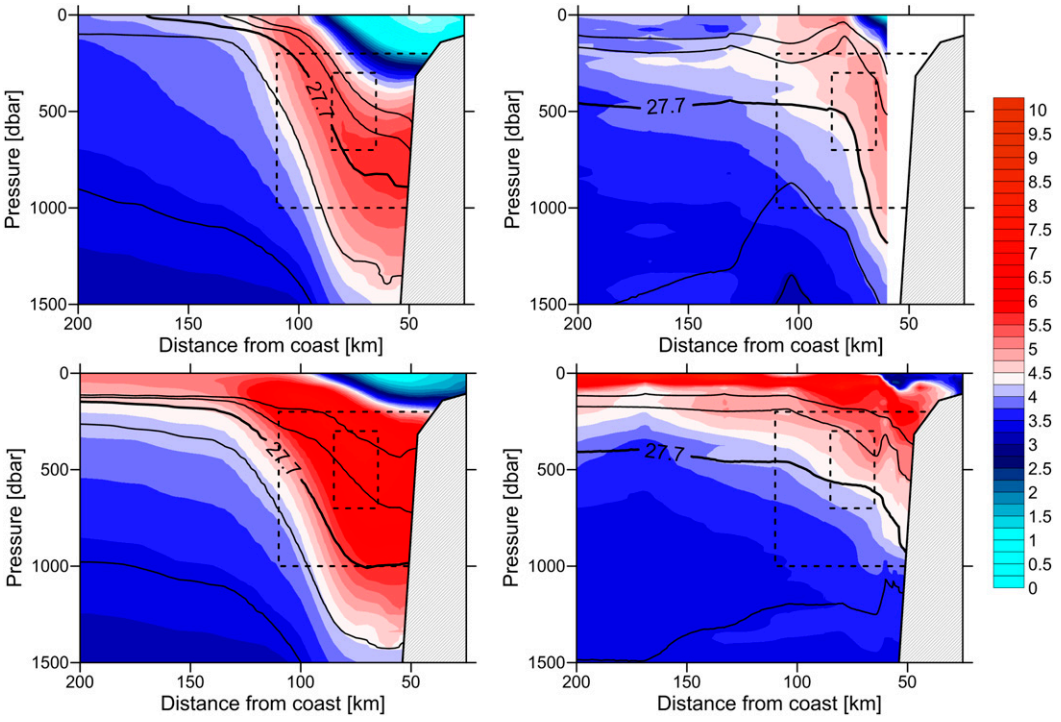

FIG. 2. Mean temperature (°C) in FLAME for (top left) May and (bottom left) August on the section. Observations from (top right) May 2008 and (bottom right) August 2008 from the AR7W section. The two definitions used to determine core temperature and salinity are also shown. The box includes the area defined as the core by Rykova et al. (2015). Here we use a second definition, between the 27.55 and 27.75 kg m^{-3} isopycnals (black lines) down to 100 km offshore.

Water in the model WGC were determined using two methods. The first is similar to the method used by Rykova et al. (2015) on the AR7W section. Mean temperature and salinity are determined with a box that encloses the core of the Irminger Water. The box extends between 300 and 700 m deep and between the Greenland slope and 20 km offshore of the slope. The second method depends less on the exact position of the IW core. It includes the water column between the 27.55 and 27.75 kg m^{-3} isopycnals between the slope and 100 km offshore. Monthly means from both methods show that the IW reaches a maximum in temperature and salinity in November/December and a minimum in May/June (Fig. 3). The range in temperature within the small box is 0.98°C while the range in salinity is 0.12. Considering the same months for which Rykova et al. (2015) had hydrographic data available, the range between the May–July and October–February mean is 0.66°C in temperature, which is very similar to their observations of a temperature range of 0.6°C. FLAME's seasonal range in salinity is 0.08, which is larger than Rykova et al.'s range of 0.01.

The timing of the peak temperature (and salinity) in late fall is related to the seasonal cycle in the source region of the IW, namely, the Irminger Sea. The temperature lags the maximum temperature of the Irminger Current on the East Greenland slope by 21 days (correlation 0.53 for salinity, 0.64 for temperature at 21 days, 95% significant). This timing agrees with the pathway and transport times of particles released at 250 m on a section upstream of the box at 59.5°N off the eastern shelf of Greenland (similar to the World Ocean Circulation Experiment repeat section AR7E, not shown). During advection around Cape Farewell the water is cooled by 0.61°C and freshened by 0.09. This decrease in T and S is likely due to boundary–interior exchange in the Cape Farewell area (Holliday et al. 2009), with a small contribution from sea-to-air fluxes.

The model WGC along the West Greenland shelf is strongest in January, with a monthly mean maximum surface velocity of 108 ± 24 cm s^{-1} and a minimum in June of 95 ± 21 cm s^{-1}. Averaged over the area between 60 and 100 km offshore (Fig. 4), the monthly means for the same months are 68 ± 16 and 58 ± 12 cm s^{-1}. The structure of the current also changes seasonally. As the isopycnals flatten in fall, the current becomes more surface intensified. The current core is quite narrow, with velocities decaying to 20 cm s^{-1} about 25 km outside the current core. The narrowness of the current is a

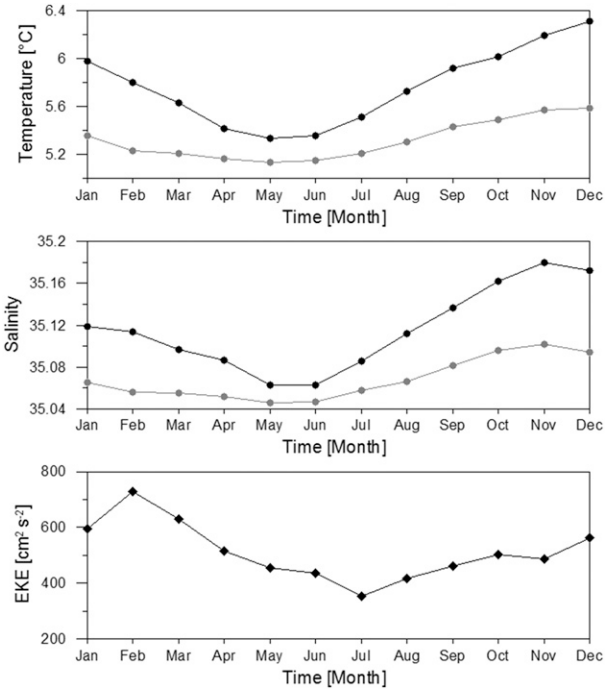

FIG. 3. Mean seasonal cycle of the Irminger Current core. The black lines shows the (top) temperature and (middle) salinity averaged over the core box defined by Rykova et al. (2015) (shown in Fig. 2). The gray lines show the averages between the 27.55 and 27.75 kg m^{-3} isopycnals down to 100 km offshore (Fig. 2). (bottom) Seasonal cycle of EKE over the horizontal box around the EKE maximum (Fig. 1).

possible explanation of why Rykova et al. (2015) found lower velocities. They derived a maximum surface velocity of 60 cm s^{-1} from the gridded AVISO altimetry product. Steep gradients are generally smoothed out in these products (Chelton et al. 2011). We will compare the FLAME volume transports in the WGC and Labrador Current further to observed values in section 3c.

The seasonal cycle of the model EKE maximum off the West Greenland shelf lags that of the velocity in the model. EKE was calculated as

$$\mathrm{EKE} = \frac{1}{2}[(u-\overline{u})^2 + (v-\overline{v})^2], \qquad (3)$$

where $\overline{u}$ and $\overline{v}$ are the time (15 years) averaged velocities. The EKE averaged over the box off the West Greenland coast exhibits a maximum in February and a minimum in July (Fig. 3). The mean values of the seasonal maximum (730 cm^2 s^{-2}) and minimum (352 cm^2 s^{-2}) agree well with the values derived from altimetry by Brandt et al. (2004), with a maximum of approximately 800 cm^2 s^{-2} and a minimum of around 400 cm^2 s^{-2}.

The shape of the region of high EKE values is similar to observations. The "lobe" of elevated EKE coming off the maximum EKE on the shelf seems somewhat more aligned with the isobaths and less directed into the deeper interior basin, but is more similar to the shape of the observed EKE (Lilly et al. 2003) than the model study by Chanut et al. (2008).

b. *The model eddies*

We will briefly discuss the eddies identified by the detection algorithm. Counting only coherent model eddies that had tracks of at least three time steps (9 days), there were on average a minimum of 17.5 eddies detected in January (9.2 anticyclones and 8.3 cyclones) and a maximum of 46.8 in July (19.9 anticyclones and 26.9 cyclones) in the study area shown in Fig. 5. In January, the eddies (both cyclones and anticyclones) are predominantly found near the eddy formation region off the West Greenland shelf and in the southeast part of the Labrador Sea, with relatively low numbers of eddies in the interior. In July, the eddies are spread more homogeneously across the Labrador Sea (Fig. 5), although higher concentrations are still found in the northern area. Eddies associated with the Irminger ring formation area, for example, tracks starting north of 60°N, are generally smaller than those in the south (mean $R = 16.1 \pm 6.4$ km versus 20.9 ± 10.6 km). Even though they are smaller, they are more energetic (Fig. 5) and northern (southern) cyclones have a mean azimuthal surface velocity of 16.2 (11.4) cm s^{-1}, while northern (southern) anticyclones have a mean azimuthal surface velocity of -33.4 (-16.4) cm s^{-1}, contributing to the high EKE in the northern part of the basin. Figure 5 is very similar to the map of eddy speeds derived by Lilly et al. (2003), with a maximum off West Greenland extending along the 3-km isobaths and into the basin, a region of slightly elevated EKE in the center and a separate elevated region in the southeast of their study area (bounded at 53°N and 44°W).

Figure 6 shows the tracks of the detected eddies. Only tracks that extend beyond 1 month are drawn. A total of 967 tracks, 346 belonging to cyclones and 621 belonging to anticyclones, are drawn. The longest anticyclone (cyclone) track is 9.5 (6.5) months. Clear bands of tracks extend from the Irminger rings formation area off the West Greenland shelf. These bands correspond with the location and banding of the EKE maximum defined by the model data. In the interior, tracks of anticyclones, which appear to circulate in a large-scale cyclonic pattern, are visible. They are very similar in radius (20.6 km) and swirl velocity (-14.4 cm s^{-1}) to the anticyclones south of 56°N (21.8 km and -14.6 cm s^{-1}, respectively), while being larger and slower than the Irminger rings (17.5 km and -21.6 cm s^{-1}, respectively). In the southwest, cyclones appear to be shed by the

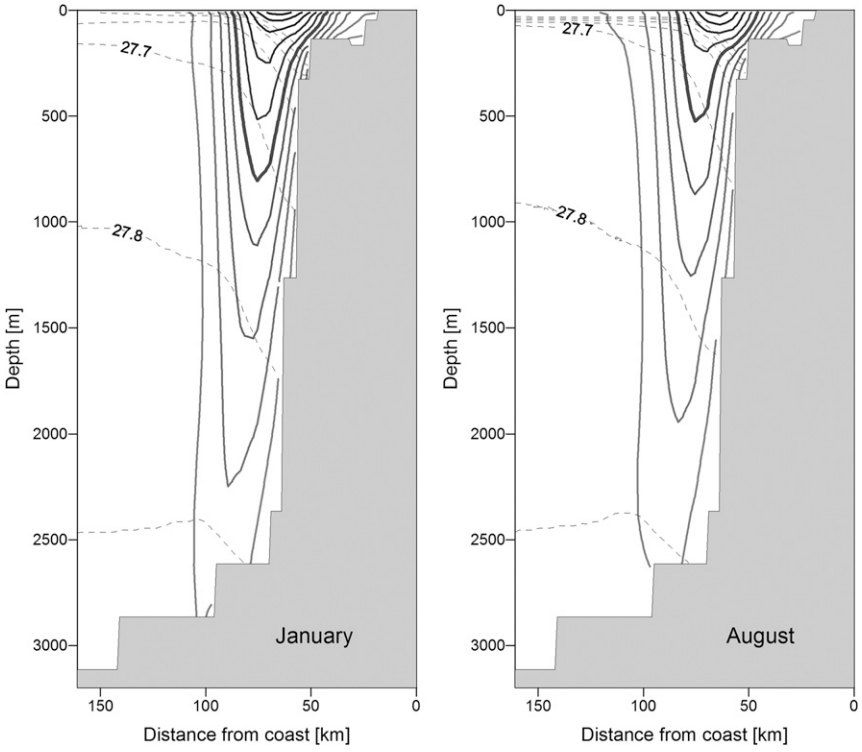

FIG. 4. Velocity structure of the WGC (left) in January when the currents are strongest and (right) in August when the currents are weakest. Isotachs are drawn every 10 cm s^{-1}, with the 50 cm s^{-1} isotach drawn thicker. Isopycnals are drawn with dashed lines.

Labrador Current and are recirculated back toward the entrance of the Labrador Sea (section CENTER; see section 3c for explanation of Labrador Sea sections).

A map of heat content relative to $T_{ref}(t)$ derived for all eddies (Fig. 7) further illuminates the different character of the Irminger rings, the eddies in the interior, and the southern eddies. The interior eddies have a significantly lower heat content, typical of eddies formed by instabilities of the convective area. The eddies in the shallow (<1 km) northern rim also have lower heat content because of their higher relative volume of cold, fresh WGC water and freshwater originating from Baffin Bay. Both the eddies along the northern boundary offshore of the 1-km isobaths and the eddies in the south have a higher heat content, consistent with an origin in the relatively warm boundary current (either the Labrador Current or possibly the Northwest Corner). In the flux calculation of the section across the entrance of the Labrador Sea, we will show that the southern eddies do not contribute significantly to the heat and freshwater fluxes into the basin. Therefore, the focus of eddy fluxes will be on the Irminger rings.

A comparison was made between the eddy observations at the IRINGS mooring in the Labrador Sea (de Jong et al. 2014) and the conditions at the same location in the FLAME model (Fig. 1). During the 2-yr deployment of the IRINGS mooring (September 2007 to September 2009), 12 anticyclones were recorded, of which 11 had distinct properties (two eddy observations spaced 10 days apart were likely the same eddy). Radii of the observed eddies varied between 11 and 35 km, with a mean radius of 21 km. Maximum azimuthal velocities varied between −50 and −14 cm s^{-1}, with a mean of −35 cm s^{-1}. In the FLAME model, 77 eddies pass within one radius distance of the IRINGS location over the 15-yr time period. Of these 77 eddies, 64 are anticyclones and 13 are cyclones. The FLAME anticyclones have mostly very similar properties as those observed. Their radii are between 11.3 and 33.3 km, with a mean of 17.8 km. Their azimuthal velocities are between −88.3 and −7.7 cm s^{-1}, with a mean of −24.6 cm s^{-1}.

c. *Mean fluxes of volume, heat, and freshwater*

While the variability of EKE is relatively easy to observe (by altimetry), the more interesting parameters with regard to the circulation and Labrador Sea Water (LSW) formation are the fluxes of volume, heat, and freshwater. Therefore, model volume, heat, and freshwater fluxes were calculated across several sections in the Labrador Sea. Three sections form a box around the

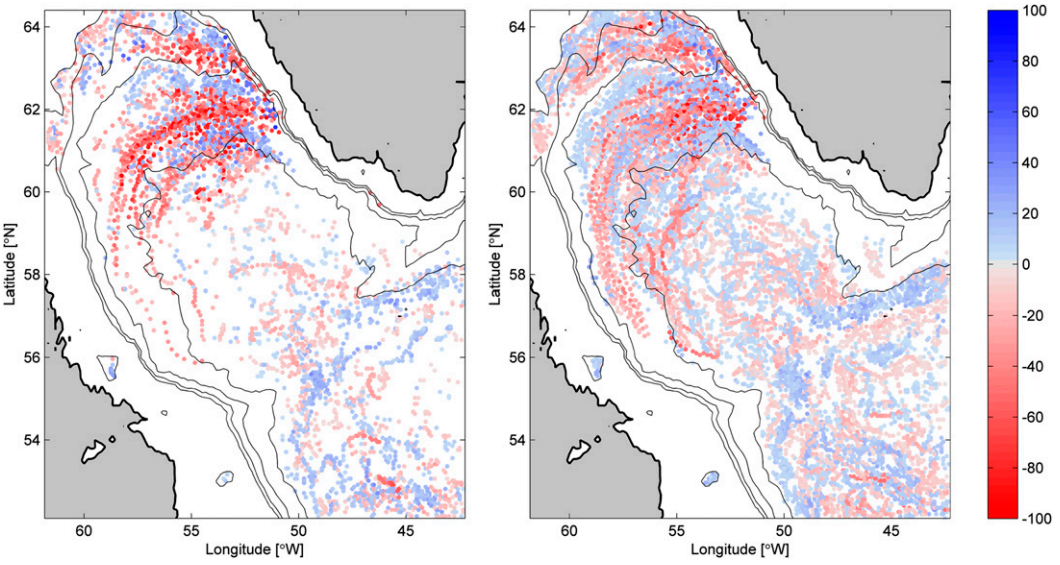

FIG. 5. Position of all eddies from 1990 to 2005 detected in (left) January/February and (right) July/August. The colors indicate the radial velocity of the eddies (cm s^{-1}), with red denoting anticyclonic circulation and blue denoting cyclonic circulation. The strongest anticyclones are seen near the Irminger rings formation area off the west coast of Greenland. Isobaths are drawn at 500, 1000, 2000, and 3000 m.

EKE maximum off West Greenland (Fig. 1). The sections on the sides of the box are called IN (southern side), OUT (northern side), and FLANK (western side). A fourth section is drawn across the entrance of the Labrador Sea. This section is divided into three parts: LC containing the Labrador Current outflow, WGC containing the Irminger Water inflow, and CENTER. Fluxes are calculated for the full depth as well as for two separate layers, from the surface to 200 m capturing the fresh West Greenland Current water expelled by the boundary current, and from 200 to 1000 m capturing the warm, saline Irminger Water expelled by the boundary current. The heat transport in Watts is defined as

$$H(t) = \iint \rho c_p [T(t) - T_{\mathrm{ref}}] v(t)\, dx\, dz, \qquad (4)$$

where $\rho = 1027\,\mathrm{kg\,m^{-3}}$ is the reference density, $c_p = 4000\,\mathrm{J\,kg^{-1}\,C^{-1}}$ is the heat capacity of seawater, $v(t)$ is the velocity across the section, $T(t)$ is the temperature at the section, and T_{ref} is a reference temperature. The transport in Sverdrups of freshwater (FSv) is defined as

$$F(t) = \iint \{1 - [S(t)/S_{\mathrm{ref}}]\} v(t)\, dx\, dz, \qquad (5)$$

where $S(t)$ is the salinity at the section and S_{ref} is a reference salinity. The values of T_{ref} and S_{ref} in Eqs. (4) and (5) are identical to those in Eqs. (1) and (2), being either fixed as the minimum of the mean seasonal cycle or $T_{\mathrm{ref}}(t)$ and $S_{\mathrm{ref}}(t)$ defined as the mean values of the convective region at time t.

Table 1 shows the partition of volume, heat, and freshwater fluxes between the sections. The full depth volume flux out of the basin in the LC is slightly larger (47.4 Sv; $1\,\mathrm{Sv} = 10^6\,\mathrm{m^3\,s^{-1}}$) than the flux through IN into the basin in the West Greenland and Irminger Current (45.3 Sv). The difference is caused by a small transport through CENTER (2.1 Sv). The net flux across the entrance of the Labrador Sea (LC + CENTER + WGC) is small (0.01 ± 0.05 Sv out of the basin). Transport at the northern boundary of our study area at 65°N, just south of Davis Strait, is negligible (0.003 Sv). The reduced transport through Davis Strait compared to observations (Curry et al. 2011, 2014) may be a result of the prescribed conditions at the northern boundary of the model (70°N). Although transport through Davis Strait is a potential source of freshwater to the interior Labrador Sea this is not a focus of this study.

As mentioned in section 3a, the FLAME volume transport in the WGC is possibly too strong. In winter (summer) the mean full depth transport between the coast and 150 km offshore in FLAME is 43 Sv (39 Sv), significantly more than the 29.1 Sv derived by Rykova et al. (2015). However, Fischer et al. (2010) estimated 41.8 ± 4.2 Sv for the total flow southward at the 53°N array on the west side of the Labrador basin, which is closer to the volume flux from FLAME (47.4 Sv). While Rykova et al. (2015) had limited hydrographic observations, mostly from summer, Fischer et al.'s (2010) estimate comes from a

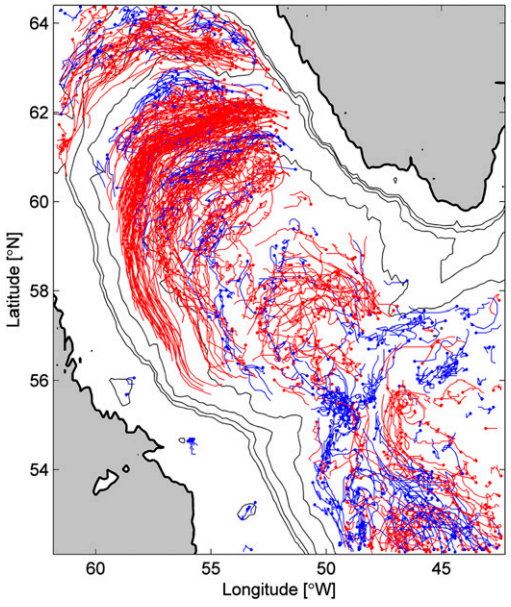

FIG. 6. Eddy tracks. Only tracks of 1 month or longer are shown. Cyclone tracks are shown in blue. Anticyclone tracks are shown in red. The first position of a track is indicated with a small dot. Isobaths are drawn at 500, 1000, 2000, and 3000 m.

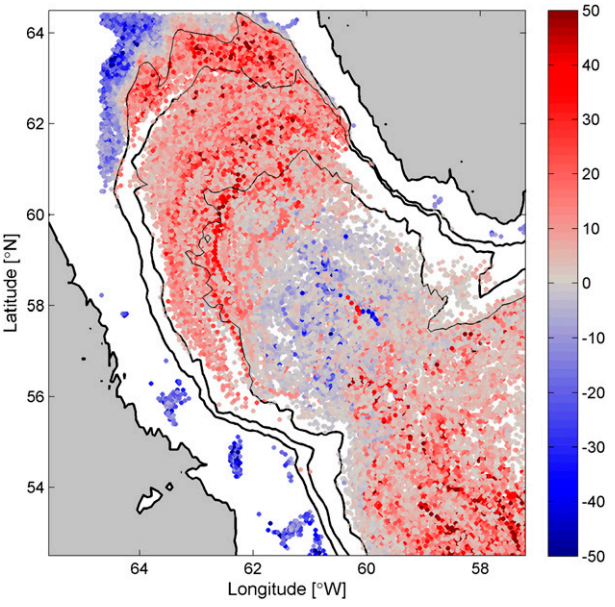

FIG. 7. Heat content of eddies (MJ m^{-2}) showing the different nature of the coherent eddies in the north, middle, and south of the basin. For this figure the heat content in the layer between 200 and 1000 m from Eq. (1) is divided by R_{LSW}^2, where R_{LSW} is the radius of the convective area (assumed to be 300 km). This transforms the heat content to a heat contribution per square meter of convective area similar to Hátún et al. (2007) and de Jong et al. (2014); both studies derived a heat contribution of about 40 MJ m^{-2} for Irminger rings.

moored array that observed the boundary current year-round between 1997 and 2009, and therefore their estimate may be more representative of the annual mean.

Most of the volume that enters the basin at the WGC section continues north through IN into the box (42.4 Sv). About 65% of this volume (27.5 Sv) is diverted through FLANK out the western side of the box and along the 3-km isobath, while the rest (14.9 Sv) continues in the shallower boundary current (OUT). These two branches are similar to the flow observed from PALACE floats (Cuny et al. 2002). The two flows merge into the boundary current along the slope of Newfoundland as the transport is back to (slightly more than) its initial strength at LC. The mean net heat flux between the surface and bottom through the section LC, CENTER, WGC equals 76.2 W m^{-2}. This approximately balances the mean surface cooling of the FLAME forcing field of 76.3 W m^{-2} over the region between 52° and 65°N and 63° and 43°W. Most of that heat comes into the basin in the WGC, which imports about 138 TW [105 TW using $T_{ref}(t)$] of heat and 10 Sv [12 Sv using $S_{ref}(t)$] of freshwater into the basin in the upper 1000 m (Table 1). Transports of heat and freshwater through Davis Strait are negligible. The division of heat and freshwater coming through IN is different for the upper 200 m and the 200–1000-m layer. In the upper 200 m, most of the heat (~80%) is diverted from the boundary current through FLANK, while most of the freshwater (~85%) continues in the boundary current through OUT around the basin. This is likely due to the fact that most of the freshwater is found on the shallow Greenland shelf and is not easily fluxed offshore, although the model IRs transport some freshwater in their caps. In the 200–1000-m layer, the heat and freshwater (or salt, as the freshwater flux is negative) is split in nearly equal parts between the broad 3-km isobaths flow and the shallower boundary current.

Despite the large increase in transport along the Newfoundland slope, the boundary current heat and freshwater fluxes change little between the northern side of the box (OUT) and the exit of the Labrador Sea at the section (LC). This suggests that most of the heat for restratification supplied by the boundary current enters the basin from the eddy formation area off the West Greenland shelf through FLANK. To estimate the extent of this exchange, the volume, heat, and freshwater fluxes across an additional section MID were calculated (Figs. 1, 8). This section is located midbasin along the axis of the basin across the main outflow through FLANK. The volume fluxes across the two sections are nearly identical (27.5 Sv through FLANK and 28.8 Sv through the additional section). However, the heat and

TABLE 1. Transports across the sections in the Labrador Sea. The numbers before the section names correspond to Fig. 1. Volume transport between the surface and bottom, heat (H), and freshwater (F) transport relative to the constant references T_{ref} and S_{ref} in the layer between the surface and 200 m and the layer between 200 and 1000 m. The sign notations are positive for northward and eastward transport of volume, heat, and freshwater.

	Volume (Sv)	H 0–200 (TW)	H 200–1000 (TW)	F 0–200 (FSv)	F 200–1000 (FSv)
Section					
1. LC	−47.4 ± 6.0	−7.9 ± 25.4	−67.4 ± 19.9	−14.4 ± 3.0	3.1 ± 1.2
2. CENTER	2.1 ± 5.5	1.6 ± 2.9	2.8 ± 3.6	0.1 ± 0.2	−0.1 ± 0.2
3. WGC	45.3 ± 5.2	26.1 ± 36.9	111.8 ± 25.0	15.5 ± 5.2	−5.0 ± 1.5
Box					
4. IN	42.4 ± 4.6	23.5 ± 35.0	110.7 ± 26.0	16.0 ± 5.2	−5.2 ± 1.7
5. FLANK	−27.5 ± 6.2	−19.2 ± 11.3	−50.3 ± 18.9	−1.3 ± 1.5	2.6 ± 1.1
6. OUT	14.9 ± 5.0	2.0 ± 22.9	54.6 ± 18.0	13.9 ± 4.2	−2.3 ± 1.2
7. MID	−28.8 ± 7.7	−16.4 ± 8.5	−39.0 ± 13.9	−0.8 ± 0.8	1.9 ± 0.8

freshwater fluxes through this section are reduced compared to FLANK. In the upper layer the heat (freshwater) flux is 85% (65%) of that of FLANK, while in the lower layer the heat (freshwater) flux is 77% (74%) of that of FLANK. Thus, significant mixing occurs offshore of the Irminger ring formation area. This is confirmed by a particle release experiment (Fig. 8). At the start of every month in the FLAME dataset, particles were released on each grid point on both the southern and northern sides of the box. The particles were tracked forward for 1 year using the 516-m horizontal flow field. Particles released on the northern side of the box mostly follow the narrow boundary current along the 2-km isobath. This is in line with the similar heat transport going through OUT at the northern end of the box and exiting the Labrador Sea through LC. The exchange between Irminger Current Water and the interior is limited to the flow over the 3-km isobaths, the western edge of the convective region, and the entrance of the Labrador Sea. Particles released on the southern, inflow side of the box spread out more over the basin. The broad main flow follows the 3-km isobath but extensive exchange with the interior appears to occur.

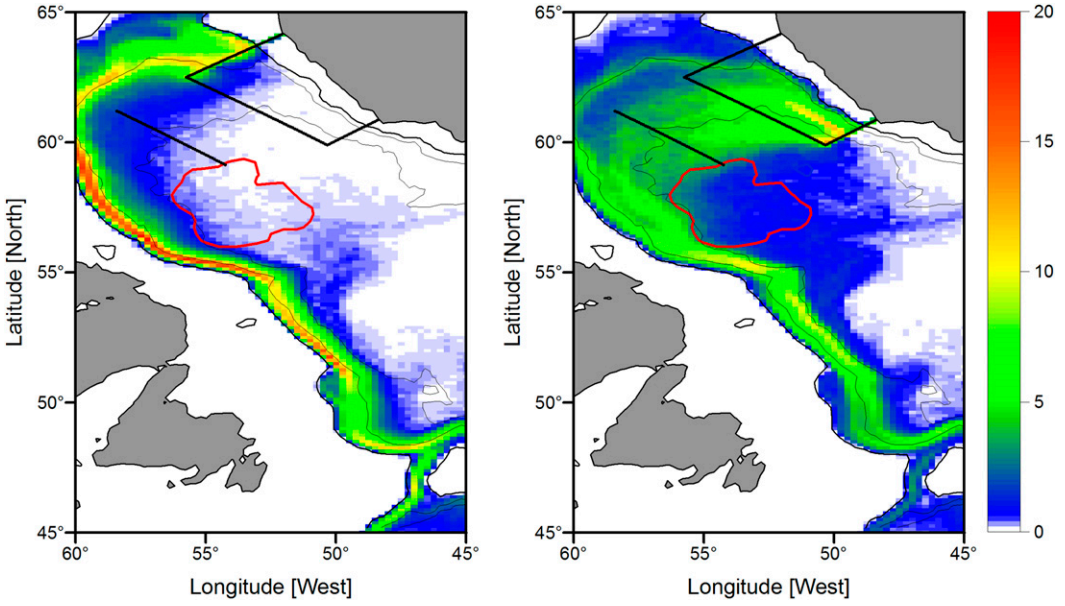

FIG. 8. Distribution of particles released at 516 m depth at (left) the northern side of the box and (right) the southern side of the box. Shown is the percent of total number of released particles that arrived at a particular 0.5° longitude × 0.25° latitude grid box. Drawn on top (black) are the box around the EKE maximum off the West Greenland coast and the additional section across the westward outflow out of the box. The red contour indicates the region of strongest convection.

TABLE 2. Transport by eddies across the western side of the box (FLANK in Table 1). Shown are N number of eddies per year and volume of the eddies in the upper 1000 m as well as the percentage of the total volume transport over the upper 1000 m, the mean of which is 12.1 Sv. Heat (H) and freshwater (F) transport are shown as their number as well as the percentage of the total transport in either the upper 200 m or between 200 and 1000 m for all eddies crossing the box, eddies with lifetimes of 1 month or longer; and eddies with lifetimes of 2 months or longer. Numbers are shown for anticyclones (AC), cyclones (CC), and both together (All).

			Surface to 200 m		200 to 1000 m	
	N (yr^{-1})	Volume (Sv)	H ($MJ\,s^{-1}$)	F ($cm\,s^{-1}$)	H ($MJ\,s^{-1}$)	F ($cm\,s^{-1}$)
			Eddies crossing the box boundary			
All	35.2	1.90 (15.7%)	2.73 (14.2%)	0.23 (17.7%)	9.07 (18.0%)	−0.36 (14.0%)
AC	20.9	1.03 (8.5%)	1.32 (6.9%)	0.18 (13.5%)	6.12 (12.2%)	−0.32 (12.3%)
CC	14.3	0.87 (7.2%)	1.41 (7.4%)	0.06 (4.3%)	2.95 (5.9%)	−0.04 (1.7%)
			Eddies with lifetimes of 1 month or longer			
All	9.5	0.58 (4.8%)	0.63 (3.3%)	0.12 (8.9%)	3.55 (7.1%)	−0.19 (7.3%)
AC	8.8	0.53 (4.4%)	0.56 (2.9%)	0.11 (8.8%)	3.40 (6.8%)	−0.18 (6.9%)
CC	0.8	0.05 (0.4%)	0.07 (0.4%)	0.00 (0.1%)	0.15 (0.3%)	−0.01 (0.4%)
			Eddies with lifetimes of 2 months or longer			
All	5.3	0.36 (3.0%)	0.39 (2.0%)	0.08 (5.9%)	2.29 (4.6%)	−0.12 (4.5%)
AC	5.1	0.34 (2.8%)	0.37 (1.9%)	0.08 (5.9%)	2.26 (4.5%)	−0.12 (4.5%)
CC	0.2	0.01 (0.0%)	0.01 (0.1%)	0.00 (0.0%)	0.03 (0.1%)	−0.00 (0.0%)

d. *Eddy fluxes, anomaly fluxes, and convergence of heat into the convective region*

The warm-core anticyclones are suggested to be an important source of heat to the cold convective region. We will attempt to quantify that contribution. Heat and freshwater contents of individual eddies were derived using Eqs. (1) and (2). Heat and freshwater content of eddies crossing a section can be transformed into a flux by summing the content of all eddies passing the section and dividing it by the length of the time series. The thus-derived mean fluxes of eddies crossing from the EKE maximum box into the interior basin are shown in Table 2.

All eddies together crossing the FLANK section are responsible for 15.7% of the total volume transport in the upper 1000 m, with a nearly equal division between cyclones and anticyclones. In the layer between 200 and 1000 m eddies transport 18% of the heat, with the anticyclones ($21\,yr^{-1}$) contributing the most. The cyclones, slightly fewer in number ($14\,yr^{-1}$) but similar in volume transport, clearly have core properties closer to the reference temperature and salinity, resulting in a smaller heat flux. Of the 35.2 eddies per year that cross FLANK, only $9.5\,yr^{-1}$ have tracks that exceed 1 month and only $5.3\,yr^{-1}$ have tracks that exceed 2 months (Table 2). Nearly all of these ''long lived'' eddies are anticyclones. Most of the longer tracks follow the isobaths and do not enter the convective region (Fig. 6). Therefore, the transport of heat to the convective region in FLAME does not seem to occur through advection of warm water cores within coherent rings.

Eddy fluxes include more than the transport by coherent rings. It is the flux of the anomalies from the mean, which also includes noncoherent (sub)mesoscale features. Therefore, we also derive eddy fluxes by Reynolds decomposition. We decomposed the temperature advection of the Labrador Sea (averaged over the upper 1 km) in a mean and eddy flux to gain insight into the relative importance of eddy variability, including both coherent and incoherent eddy motions. To avoid confusion with the flux derived from the heat and salt content of the coherent eddies discussed earlier, we will call the eddy flux derived from this decomposition the ''anomaly flux.'' Using the temperature and velocity fields, the temperature advection is calculated as

$$\overline{vT(x,y)} = \overline{v}(x,y)\overline{T}(x,y) + \overline{v'(x,y,t)T'(x,y,t)}, \quad (6)$$

where $\overline{v}$ and $\overline{T}$ are the long-term mean (model record) temperature and velocity at each grid point and v' and T' are the anomalies from the mean at each time step at that grid point. Figure 9 shows vectors of the mean and anomaly temperature advection as well as contours of the divergence of the heat flux calculated as

$$\text{Divergence} = \rho c_p \nabla \cdot vT. \quad (7)$$

The map shows that the mean temperature advection is mostly along isobaths, while the anomaly temperature advection has a large cross-isobath component near the EKE maximum. Even though the anomaly temperature advection is much smaller in magnitude than that of the mean fields, the anomaly heat flux convergence in the convective region (responsible for local warming) is higher. The mean flow does contribute some warming of the convective region along its western edge. The banding of cooling and warming regions along the northern side

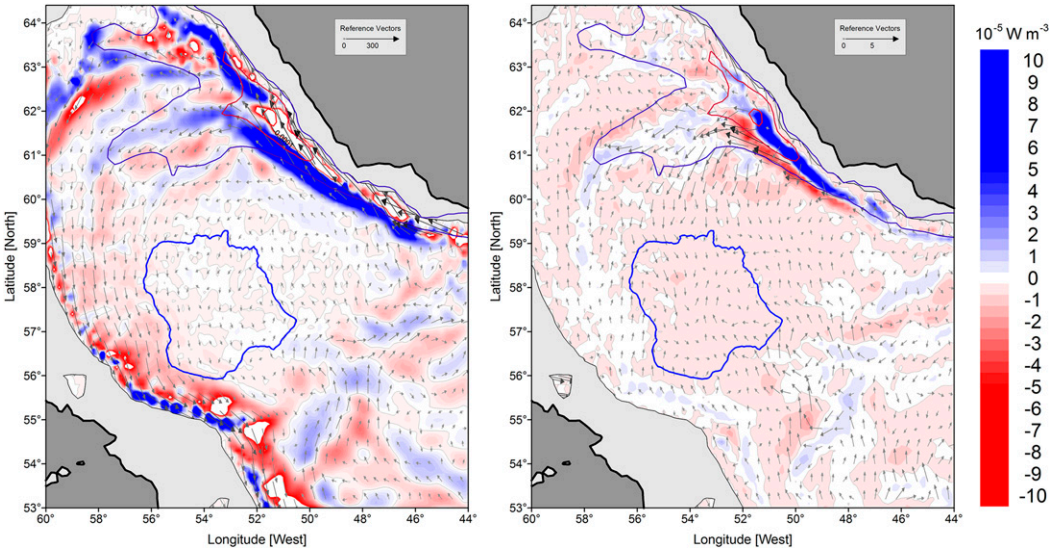

FIG. 9. Mean fields for temperature advection (vectors) and heat flux divergence (contours). (left) Advection and divergence of the mean field and (right) advection and divergence of the eddy field. Convergence (negative divergence) is coded red to indicate warming. Contours of EKE from Fig. 2 are drawn, as well as the boundary of the convective region.

of the basin seems to coincide with the bands of cyclone and anticyclone tracks in Fig. 6.

Equation (7) can also be applied to construct a monthly mean climatology rather than a mean over the 15-yr time series. For each month the heat flux divergence in the convective region for the mean and anomaly flux components was calculated. The boundary of the convective region (Fig. 8) was defined as the smoothed contour of the mean maximum mixed layer depth of 1500 m. Figure 10 shows the monthly climatologies of this region. During the months with the strongest surface forcing (January–March; Fig. 10), the heat convergence by the mean flow is low and that of the anomaly heat flux is increasing but not enough to balance the surface cooling. In April the surface cooling and lateral heat convergence balance and the mean temperature of the convective region remains steady. In May–October the surface forcing is weaker ($<100\,\mathrm{W\,m^{-2}}$) and the basin warms. The reduced convergence by the anomaly flux is thought to be related to the decreasing EKE values and less Irminger rings formation during these months. The heat convergence by the mean flow gradually increases because of overall heating of the basin through spring and summer but remains smaller than the anomaly fluxes through most of the year.

We conclude that though coherent eddies, especially anticyclones, are effective at transporting properties, they apparently are not the most important mechanism for transport from the WGC into the convective region in the FLAME model. The coherent eddies are too small and too few to transport the bulk of heat needed for restratification. Even so, the instability in the boundary current creates a strong cross-isobath flow, providing heat to the interior. Eddies and other mesoscale features provide further mixing of boundary current water and interior water along the 3-km isobaths.

e. *Interannual variability*

Little is known about the interannual variability in Irminger rings. Lilly et al. (2003) described a decrease in the number of anticyclones at the Bravo mooring during years of strong convection. This mooring was located farther away from the Irminger rings formation area (Fig. 1). These authors suggested that the anticyclones' warm core may get destroyed by convective mixing more quickly in strong winters, weakening the eddies and shortening their lifetime. Brandt et al. (2004) described interannual variability of the EKE in the Labrador Sea. In the mid-1990s (1994–96), the baseline EKE (or the minimum annual EKE) was high but the amplitude of the seasonal cycle was smaller than average. From 1997 to 2001, the amplitude of the seasonal cycle increased, leading to higher maxima in winter and lower minima in summer. Brandt et al. (2004) suggested that these changes were due to changes in the density difference between the interior and the boundary as a result of convection, as well as to changes in the wind stress curl driving the boundary current. We will study the interannual variability in FLAME in more detail here.

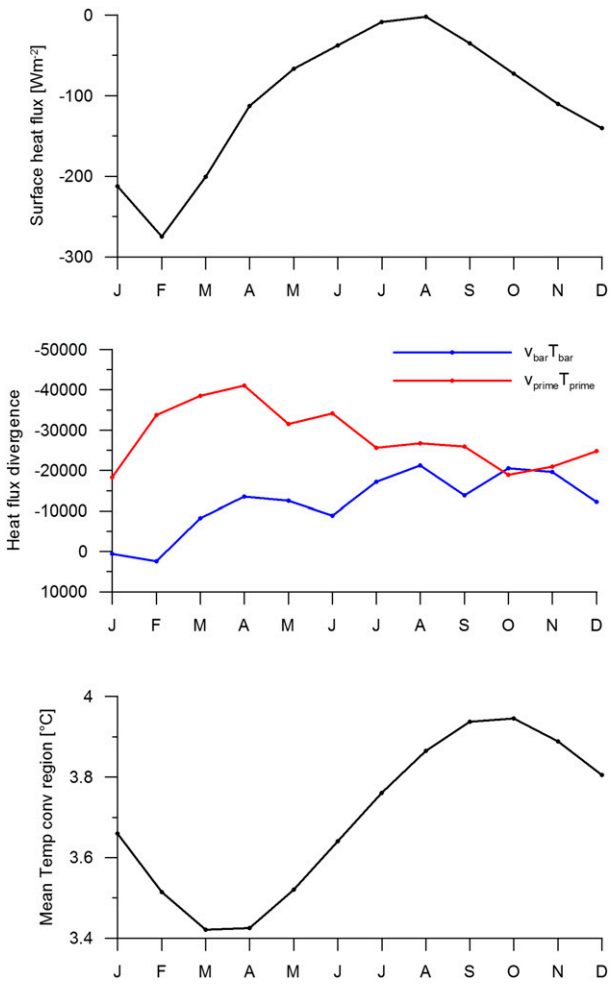

FIG. 10. Monthly climatologies of (top) FLAME surface heat fluxes, (middle) heat flux divergence of the mean (blue) and eddy (red) fields, and (bottom) spatially (within convective area drawn in Fig. 9) and vertically (1 km) averaged temperature of the convective region.

Not surprisingly, the seasonal cycle is dominant in all model fields (e.g., T, S, heat, and freshwater fluxes), but some interannual variability is also apparent in the 15-yr model time series. Figure 11 shows the variability of the maximum mixed layer depth (MLD) in the central Labrador Sea. The maximum MLD was determined as the depth where density exceeded the surface density by $0.005\,\mathrm{kg\,m^{-3}}$, similar to Chanut et al. (2008). While the variability is not as large as observed (Yashayaev 2007), FLAME does show similar tendencies, with mixing down to nearly 2000 m in 1994 and shallower mixing in the late 1990s. However, changes in convective activity are more apparent in the areal extent of deep mixing than in maximum MLD (Fig. 11).

Convection, through densification of the interior basin, affects the density gradient that is proportional to the strength of the boundary current. Spall (2004) used a conceptual model to show the dependence of the eddy heat fluxes from the boundary current on the density gradient between the boundary current and the interior. While his simple model had a varying interior density (due to convection), the boundary current density itself was held fixed. We derived time series for the density of the boundary current and the interior from the section spanning the width of the Labrador Sea in FLAME (Fig. 1). For the density of the boundary current we average the density over the region between 40 and 125 km offshore and 1000 m deep. This region envelopes the area of downward sloping (toward the boundary) isopycnals associated with the boundary current (Figs. 2, 4). For the density of the interior we average the density over a region 100 km wide and 1000 m deep in the region where the isopycnals outcrop in winter. In FLAME the range of the seasonal cycle in the boundary current density ($0.121\,\mathrm{kg\,m^{-3}}$) is in fact nearly twice as large as that of the interior ($0.067\,\mathrm{kg\,m^{-3}}$). Since the two seasonal cycles are not in phase, this results in a stronger total density gradient ($\Delta\rho$; Fig. 12) and a lagged peak gradient. In the simple model, peak density gradients would occur in March, at the end of the convective season. In FLAME the boundary current is densest in May, reducing the gradient in spring. As a result the density gradient is strongest in October, when the boundary current is most buoyant (described earlier in section 3a).

The EKE correlates strongly with both the density gradient ($R = 0.70$ with $\Delta\rho$ leading by about 2 months; Fig. 13) as well as with the maximum surface velocity $V_{\max}$ of the WGC ($R = 0.66$ with $V_{\max}$ leading by 1 month). However, after removing the seasonal cycle by computing annual means, the correlation between EKE and $\Delta\rho$ remains high (0.77). The interannual correlation between EKE and $V_{\max}$ drops to 0.24, likely because of the influence of interannual variability in wind forcing. Generally, the heat flux into the Labrador Sea (through IN and IC) shows a similar variability as $\Delta\rho$ (Fig. 13), with a correlation of the annual mean series of 0.70. However, it is unclear why 1997, a year characterized by high values of $\Delta\rho$, did not result in a higher heat flux. This year did not stand out in either wind forcing or convective activity. To look at these details is beyond the scope of this study.

The interannual variability of $\Delta\rho$, marked by a gradual increase over the 15-yr record, is predominantly determined by the increase in temperature of the boundary current, similar to what was observed in the hydrographic records of the Labrador and Irminger Seas (van Aken et al. 2011). This results in an increase in

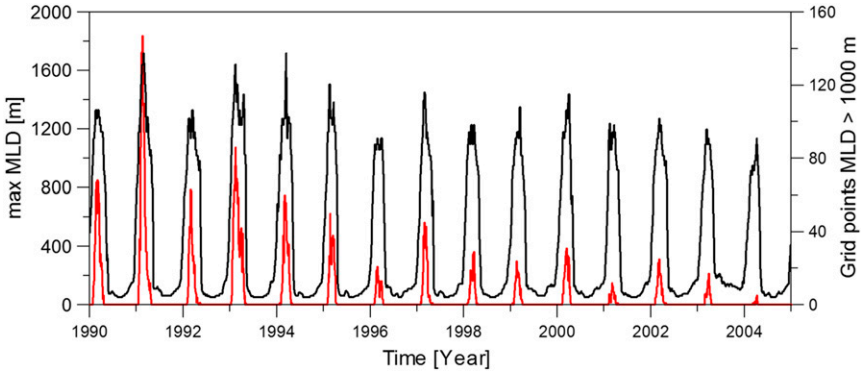

FIG. 11. Time series of maximum MLD and extent of the deep mixing area in the central Labrador Sea. The MLD (black) was determined for the region between 49° and 60°W and 55.5° and 60°N. The number of grid points exhibiting MLD > 1000 (red) is a second indicator of the convective activity.

heat fluxes from the boundary current to the interior when using a fixed reference temperature. Since the temperature of the interior basin is also increasing during this time period, the trend in the heat transport relative to $T_{\mathrm{ref}}(t)$ might be a more useful metric. Accounting for the variability in the convective region reduces seasonal cycle, but most importantly the interannual trend (Fig. 13). This is similar to the synchronous trend in eddy heat content and interior temperature observed by Rykova et al. (2009). We will discuss this in more detail later.

We note that stronger density gradients and higher EKE do not necessarily translate to more coherent eddies. To identify the effect of higher or lower EKE on Irminger ring formation, we compare two periods. The first period is January 1997 to December 1998, during which the highest values of EKE were seen in FLAME (Fig. 13). The second period is January 2000 to December 2001, during which the seasonal variability of EKE was low. About an equal number of tracks were found for these periods (142 versus 140). However, anticyclones along the 1997–98 northern tracks are slightly

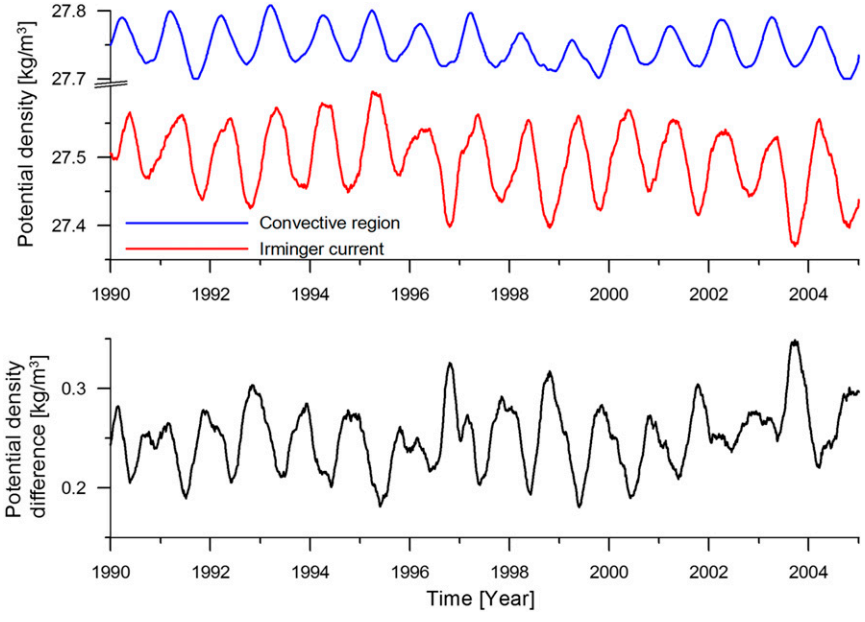

FIG. 12. (top) Time series of potential density of the upper 1000 m of the convective area and the Irminger current. (bottom) Time series of resulting density difference between the boundary current and the interior. Time series are low-pass filtered with a 3-month window.

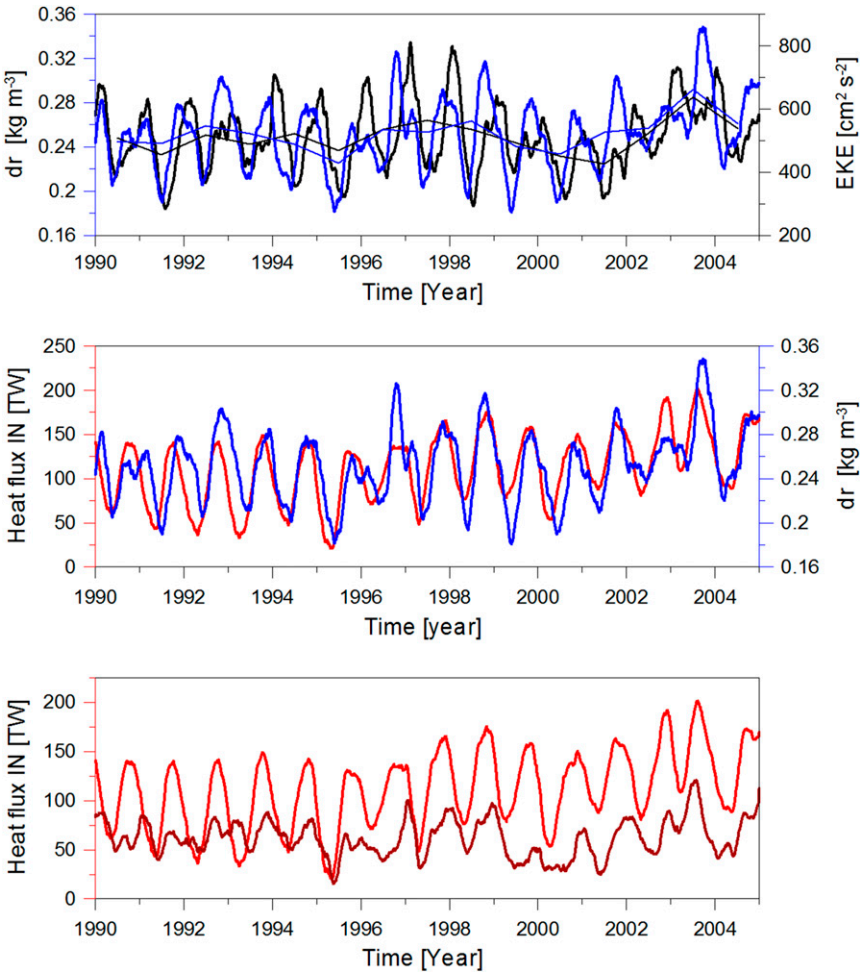

FIG. 13. (top) Time series of density difference between the boundary and the interior in blue and the EKE in black. (middle) Time series of the density difference between the boundary current and the interior in blue and the heat flux into the box between 200 and 1000 m calculated using a fixed reference temperature in red. (bottom) Heat flux into the box between 200 and 1000 m calculated using a fixed reference temperature in red and using the time-varying temperature of the interior in dark red. Time series are low-pass filtered with a 3-month window.

larger (radius of 18.9 km versus 17.1 km) and significantly more energetic (-45.7 versus -33.6 cm s^{-1}). The combination of more tightly packed tracks in the northern Labrador Sea (Fig. 6) in combination with higher swirl velocities may explain the higher EKE without a large difference in eddy numbers.

4. Discussion

Using the FLAME model we found that the Irminger rings formation area is the largest source of heat to the interior Labrador Sea. Coherent eddies transport 18% of the heat in the upper 1 km coming out of the box on the west coast of Greenland. Very few (8 in 15 years) of coherent eddies make it to the convective region. However, large transport of heat is facilitated by eddy fluxes, as is shown by decomposition of the temperature advection fields. The heat convergence in the convective region by the mean flow increases from February to October, generally following trend with the temperature within the basin, but remains lower than that of the eddy fluxes most of the year. The heat convergence by eddy fluxes peaks in April and then declines toward October. The stronger late winter eddy heat convergence facilitates restratification after convection. Since the heat transport by coherent eddies is relatively low, we must assume that this heat diverges mainly from the boundary current in noncoherent mesoscale features (filaments,

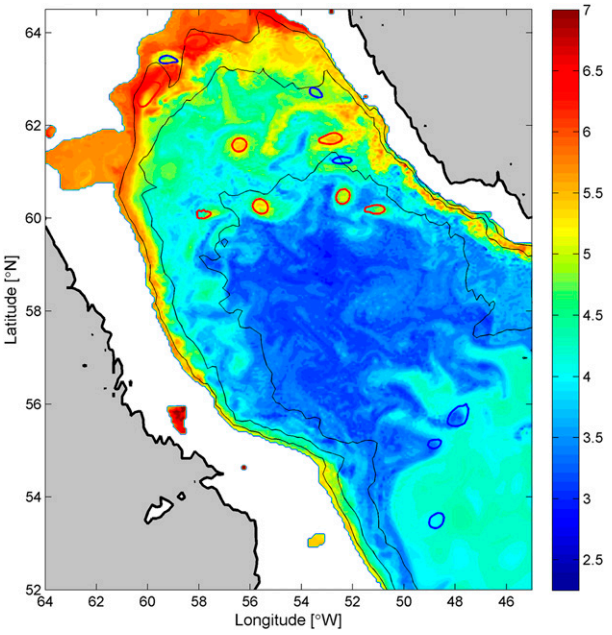

FIG. 14. Snapshot on 2 Apr 1994 of the temperature field at 500 m. Warm cores are seen to be shed from the Irminger rings formation area west of Greenland. However, many heat carrying anomalies, including a large, warm filament coming off the WGC, are not contained within the coherent rings.

short lived eddies, etc.). Even though the heat content of coherent eddies is relatively large compared to its environment, they constitute only a small part of the total surface area compared to the more ubiquitous noncoherent anomalies (Fig. 14).

Palter et al. (2008) also found the Irminger rings formation region to be an important source of heat in observations. They studied Profiling Autonomous Lagrangian Circulation Explorer (PALACE) float tracks to elucidate cross-isobath exchange along the boundary current. They found a higher ratio of PALACE floats crossing isobaths in the region of high EKE off the West Greenland shelf as well as higher ratios in winter when the EKE is at a maximum similar to the FLAME results. The shape of the observed altimeter-derived EKE maximum, extending more southward than westward, suggests that perhaps a higher number of coherent eddies makes it to the convective region in the real ocean compared to the model. Even so, it is likely that the contribution of the noncoherent anomalies to the convergence of heat is still important in the real ocean, similar to FLAME. The 2-yr time series at the IRINGS mooring (de Jong et al. 2014) showed few coherent rings (12) against a constantly fluctuating background.

The 15-yr reanalysis forcing applied to the FLAME model run allowed for an analysis of the interannual variability. We found similar variability and trends in the density gradient between the Labrador Sea interior and the boundary current, the EKE, and the heat transport in the boundary current. In FLAME interannual density changes in the boundary current are significantly larger than those in the interior, making the boundary current variability dominant in setting the gradient. These changes are likely driven by variability in either advection or air–sea interaction upstream of the Labrador Sea. Density changes in the interior are smaller because of the depth of convection in the Labrador Sea, which distributes the surface buoyancy flux vertically. However, on longer time scales (>10 years), we might expect the interior and the boundary current density to vary synchronously. This is because the Labrador Sea and the Irminger Sea, where Irminger Water is (trans)formed, are seen to show matching trends in temperature and salinity during the hydrographic record (van Aken et al. 2011). In FLAME, both the interior and boundary current showed a similar steady increase in temperature over the 15 years. When the increase in temperature in the interior was taken into account in T_{ref}, the FLAME heat flux from the boundary to the interior was steady.

The relation between the density gradient and eddy fluxes is similar to the model proposed by Spall (2004) in his idealized study. However, in Spall's model the fixed boundary current resulted in a dominance of the convective region in setting the density gradient. Our results are also in line with the conclusion of Luo et al. (2011) that the variability of EKE in the Labrador Sea is externally forced (their boundary current was prescribed at the eastern end of their ROMS domain at 35°W). Although there are long (60 years) time series describing the properties of the interior Labrador Sea, we currently have only limited observations from the boundary current, making it difficult to obtain a time series of the cross-basin density gradient. However, in July 2014 a moored array was deployed across the WGC as part of OSNAP. This will allow for some first calculations of alongshore heat transport by the boundary current. A parameterized heat transport from the boundary to the interior Labrador Sea based on time series from the interior as well as the boundary current could then be derived. Sustaining the observations of the interior, as they have been since the 1950s, as well as the new boundary current array would surely be more feasible than observing the heat transport by individual eddies. Even so, efforts should be made to observe the heat flux from the boundary to the interior to validate these model results. Current generations of global climate models (GCMs) do not have the resolution required to simulate fluxes by (sub)mesoscale processes. Saenko et al. (2014) compared high ($^1/_{12}$°) and low (1°) models in the Labrador Sea and concluded that the eddy

parameterization in the low-resolution models is not sufficient to simulate the heat exchange in the Irminger rings formation area. Consequently, reduced restratification by the boundary current could be a possible reason why some GCMs highly overestimate convective mixing in the Labrador Sea (de Jong et al. 2009).

Acknowledgments. The authors were supported in this work by the U.S. National Science Foundation. We are grateful to Claus Böning (GEOMAR, Germany) for providing the FLAME model output. We kindly thank Ross Hendry and Igor Yashayaev (BIO, Canada) and Sheldon Bacon and Penny Holliday (NOC, United Kingdom) for monitoring the AR7W sections shown in Fig. 2.

REFERENCES

Biastoch, A., C. W. Böning, J. Getzlaff, J. M. Molines, and G. Madec, 2008: Causes of interannual–decadal variability in the meridional overturning circulation of the midlatitude North Atlantic Ocean. *J. Climate*, **21**, 6599–6615, doi:10.1175/2008JCLI2404.1.

Bower, A. S., M. S. Lozier, S. F. Gary, and C. W. Böning, 2009: Interior pathways of the North Atlantic meridional overturning circulation. *Nature*, **459**, 243–248, doi:10.1038/nature07979.

——, ——, and ——, 2011: The export of Labrador Sea Water from the subpolar North Atlantic: A Lagrangian perspective. *Deep-Sea Res. II*, **58**, 1798–1818, doi:10.1016/j.dsr2.2010.10.060.

——, R. M. Hendry, D. E. Amrhein, and J. M. Lilly, 2013: Direct observations of formation and propagation of subpolar eddies into the subtropical North Atlantic. *Deep-Sea Res. II*, **85**, 15–41, doi:10.1016/j.dsr2.2012.07.029.

Bracco, A., and J. Pedlosky, 2003: Vortex generation by topography in locally unstable baroclinic flows. *J. Phys. Oceanogr.*, **33**, 207–219, doi:10.1175/1520-0485(2003)033<0207:VGBTIL>2.0.CO;2.

Brandt, P., F. A. Schott, A. Funk, and C. S. Martins, 2004: Seasonal to interannual variability of the eddy field in the Labrador Sea from satellite altimetry. *J. Geophys. Res.*, **109**, C02028, doi:10.1029/2002JC001551.

Burkholder, K. C., and M. S. Lozier, 2011: Subtropical to subpolar pathways in the North Atlantic. *J. Geophys. Res.*, **116**, C07017, doi:10.1029/2010JC006697.

Chanut, J., B. Barnier, W. Large, L. Debreu, T. Penduff, J. M. Molines, and P. Mathiot, 2008: Mesoscale eddies in the Labrador Sea and their contribution to convection and restratification. *J. Phys. Oceanogr.*, **38**, 1617–1643, doi:10.1175/2008JPO3485.1.

Chelton, B. D., M. G. Schlax, and R. M. Samelson, 2011: Global observations of nonlinear mesoscale eddies. *Prog. Oceanogr.*, **91**, 167–216, doi:10.1016/j.pocean.2011.01.002.

Cuny, J., P. B. Rhines, P. P. Niiler, and S. Bacon, 2002: Labrador Sea boundary currents and the fate of the Irminger Sea Water. *J. Phys. Oceanogr.*, **32**, 627–647, doi:10.1175/1520-0485(2002)032<0627:LSBCAT>2.0.CO;2.

Curry, B., C. M. Lee, and B. Petrie, 2011: Volume, freshwater, and heat fluxes through Davis Strait, 2004–05. *J. Phys. Oceanogr.*, **41**, 429–436, doi:10.1175/2010JPO4536.1.

——, ——, ——, R. E. Moritz, and R. Kwok, 2014: Multiyear volume, liquid freshwater, and sea ice transports through Davis Strait, 2004–10. *J. Phys. Oceanogr.*, **44**, 1244–1266, doi:10.1175/JPO-D-13-0177.1.

Czeschel, L., 2004: The role of eddies for the deep water formation in the Labrador Sea. Ph.D. thesis, Christian-Albrechts University, 96 pp.

Danabasoglu, G., S. G. Yeager, Y. O. Kwon, J. J. Tribbia, A. S. Phillips, and J. W. Hurrell, 2012: Variability of the Atlantic meridional overturning circulation in CCSM4. *J. Climate*, **25**, 5153–5172, doi:10.1175/JCLI-D-11-00463.1.

de Jong, M. F., S. S. Drijfhout, W. Hazeleger, H. M. van Aken, and C. A. Severijns, 2009: Simulations of hydrographic properties in the northwestern North Atlantic Ocean in coupled climate models. *J. Climate*, **22**, 1767–1786, doi:10.1175/2008JCLI2448.1.

——, A. S. Bower, and H. H. Furey, 2014: Two years of observations of warm-core anticyclones in the Labrador Sea and their seasonal cycle in heat and salt stratification. *J. Phys. Oceanogr.*, **44**, 427–444, doi:10.1175/JPO-D-13-070.1.

Dickson, R. R., J. Meincke, S.-A. Malmberg, and A. J. Lee, 1988: The "great salinity anomaly" in the northern North Atlantic 1968–1982. *Prog. Oceanogr.*, **20**, 103–151, doi:10.1016/0079-6611(88)90049-3.

Eden, C., and C. W. Böning, 2002: Sources of eddy kinetic energy in the Labrador Sea. *J. Phys. Oceanogr.*, **32**, 3346–3363, doi:10.1175/1520-0485(2002)032<3346:SOEKEI>2.0.CO;2.

Fischer, J., M. Visbeck, R. Zantopp, and N. Nunes, 2010: Interannual to decadal variability of outflow from the Labrador Sea. *Geophys. Res. Lett.*, **37**, L24610, doi:10.1029/2010GL045321.

Fratantoni, P. S., and R. S. Pickart, 2007: The western North Atlantic shelfbreak current system in summer. *J. Phys. Oceanogr.*, **37**, 2509–2533, doi:10.1175/JPO3123.1.

Gary, S. F., M. S. Lozier, C. Böning, and A. Biastoch, 2011: Deciphering the pathways for the deep limb of the meridional overturning circulation. *Deep-Sea Res. II*, **58**, 1781–1797, doi:10.1016/j.dsr2.2010.10.059.

Gelderloos, R., C. A. Katsman, and S. S. Drijfhout, 2011: Assessing the role of three eddy types in restratifying the Labrador Sea after deep convection. *J. Phys. Oceanogr.*, **41**, 2102–2119, doi:10.1175/JPO-D-11-054.1.

Haine, T., and Coauthors, 2008: North Atlantic Deep Water formation in the Labrador Sea, recirculation through the Subpolar Gyre, and discharge to the Subtropics. *Arctic–Subarctic Ocean Fluxes*, R. R. Dickson, J. Meincke, and P. Rhines, Eds., Springer, 653–701, doi:10.1007/978-1-4020-6774-7_28.

Hátún, H., C. C. Eriksen, and P. B. Rhines, 2007: Buoyant eddies entering the Labrador Sea observed with gliders and altimetry. *J. Phys. Oceanogr.*, **37**, 2838–2854, doi:10.1175/2007JPO3567.1.

Holliday, N. P., S. Bacon, J. T. Allen, and E. L. McDonagh, 2009: Circulation and transport in the western boundary currents at Cape Farewell, Greenland. *J. Phys. Oceanogr.*, **39**, 1854–1870, doi:10.1175/2009JPO4160.1.

Katsman, C. A., M. A. Spall, and R. S. Pickart, 2004: Boundary current eddies and their role in the restratification of the Labrador Sea. *J. Phys. Oceanogr.*, **34**, 1967–1983, doi:10.1175/1520-0485(2004)034<1967:BCEATR>2.0.CO;2.

Kieke, D., and I. Yashayaev, 2015: Studies of Labrador Sea Water formation and variability in the subpolar North Atlantic in the light of international partnership and collaboration. *Prog. Oceanogr.*, **132**, 220–232, doi:10.1016/j.pocean.2014.12.010.

——, M. Rhein, L. Stramma, W. M. Smethie, D. A. LeBel, and W. Zenk, 2006: Changes in the CFC inventories and formation

rates of upper Labrador Sea Water, 1997–2001. *J. Phys. Oceanogr.*, **36**, 64–86, doi:10.1175/JPO2814.1.

Lab Sea Group, 1998: The Labrador Sea Deep Convection Experiment. *Bull. Amer. Meteor. Soc.*, **79**, 2033–2058, doi:10.1175/1520-0477(1998)079<2033:TLSDCE>2.0.CO;2.

Lazier, J., 1980: Oceanographic conditions at Ocean Weather Ship *Bravo*, 1964–1974. *Atmos.–Ocean*, **18**, 227–238, doi:10.1080/07055900.1980.9649089.

——, R. Hendry, A. Clarke, I. Yashayaev, and P. Rhines, 2002: Convection and restratification in the Labrador Sea, 1990– 2000. *Deep-Sea Res. I*, **49**, 1819–1835, doi:10.1016/S0967-0637(02)00064-X.

Levitus, S., and T. P. Boyer, 1994: *Temperature*. Vol. 4, *World Ocean Atlas 1994*, NOAA Atlas NESDIS 4, 117 pp.

——, R. Burgett, and T. P. Boyer, 1994: *Salinity*. Vol. 3, *World Ocean Atlas 1994*, NOAA Atlas NESDIS 3, 99 pp.

Lilly, J. M., and P. B. Rhines, 2002: Coherent eddies in the Labrador Sea observed from a mooring. *J. Phys. Oceanogr.*, **32**, 585–598, doi:10.1175/1520-0485(2002)032<0585:CEITLS>2.0.CO;2.

——, ——, F. Schott, K. Lavender, J. Lazier, U. Send, and E. D'Asaro, 2003: Observations of the Labrador Sea eddy field. *Prog. Oceanogr.*, **59**, 75–176, doi:10.1016/j.pocean.2003.08.013.

Lozier, M. S., S. F. Gary, and A. S. Bower, 2013: Simulated pathways of the overflow waters in the North Atlantic: Subpolar to subtropical export. *Deep-Sea Res. II*, **85**, 147–153, doi:10.1016/j.dsr2.2012.07.037.

Luo, H., A. Bracco, and E. Di Lorenzo, 2011: The interannual variability of the surface eddy kinetic energy in the Labrador Sea. *Prog. Oceanogr.*, **91**, 295–311, doi:10.1016/j.pocean.2011.01.006.

Manabe, S., and R. J. Stouffer, 1995: Simulation of abrupt climatic change induced by freshwater input to the North Atlantic Ocean. *Nature*, **378**, 165–167, doi:10.1038/378165a0.

Myers, P. G., N. Kulan, and M. H. Ribergaard, 2007: Irminger Water variability in the West Greenland Current. *Geophys. Res. Lett.*, **34**, L17601, doi:10.1029/2007GL030419.

Nencioli, F., C. Dong, T. Dickey, L. Washburn, and J. C. McWilliams, 2010: A vector geometry–based eddy detection algorithm and its application to a high-resolution numerical model product and high-frequency radar surface velocities in the Southern California Bight. *J. Atmos. Oceanic Technol.*, **27**, 564–579, doi:10.1175/2009JTECHO725.1.

Pacanowski, R. C., 1996: MOM 2 documentation user's guide and reference manual. GFDL Ocean Tech. Rep. 3.2, 329 pp. [Available online at http://www.gfdl.noaa.gov/cms-filesystem-action/model_development/ocean/manual2.2.pdf.]

Palter, J. B., M. S. Lozier, and K. Lavender, 2008: How does Labrador Sea Water enter the Deep Western Boundary Current? *J. Phys. Oceanogr.*, **38**, 968–983, doi:10.1175/2007JPO3807.1.

Pickart, R. S., D. J. Torres, and R. A. Clarke, 2002: Hydrography of the Labrador Sea during active convection. *J. Phys. Oceanogr.*, **32**, 428–457, doi:10.1175/1520-0485(2002)032<0428:HOTLSD>2.0.CO;2.

Prater, M. D., 2002: Eddies in the Labrador Sea as observed by profiling RAFOS floats and remote sensing. *J. Phys. Oceanogr.*, **32**, 411–427, doi:10.1175/1520-0485(2002)032<0411:EITLSA>2.0.CO;2.

Rhein, M., and Coauthors, 2002: Labrador Sea Water: Pathways, CFC inventory, and formation rates. *J. Phys. Oceanogr.*, **32**, 648–665, doi:10.1175/1520-0485(2002)032<0648:LSWPCI>2.0.CO;2.

Rykova, T., F. Straneo, J. Lilly, and I. Yashayaev, 2009: Irminger Current anticyclones in the Labrador Sea observed in the hydrographic record, 1990–2004. *J. Mar. Res.*, **67**, 361–384, doi:10.1357/002224009789954739.

——, ——, and A. S. Bower, 2015: Seasonal and interannual variability of the West Greenland Current System in the Labrador Sea in 1993–2008. *J. Geophys. Res. Oceans*, **120**, 1318–1332, doi:10.1002/2014JC010386.

Rypina, I. I., L. J. Pratt, and M. S. Lozier, 2011: Near-surface transport pathways in the North Atlantic Ocean. *J. Phys. Oceanogr.*, **41**, 911–925, doi:10.1175/2011JPO4498.1.

——, I. Kamenkovich, P. Berloff, and L. J. Pratt, 2012: Eddy-induced particle dispersion in the near-surface North Atlantic. *J. Phys. Oceanogr.*, **42**, 2206–2228, doi:10.1175/JPO-D-11-0191.1.

Saenko, O. A., F. Dupont, D. Yang, P. G. Myers, I. Yashayaev, and G. C. Smith, 2014: Role of resolved and parameterized eddies in the labrador sea balance of heat and buoyancy. *J. Phys. Oceanogr.*, **44**, 3008–3032, doi:10.1175/JPO-D-14-0041.1.

Spall, M. A., 2004: Boundary currents and water mass transformation in marginal seas. *J. Phys. Oceanogr.*, **34**, 1197–1213, doi:10.1175/1520-0485(2004)034<1197:BCAWTI>2.0.CO;2.

Straneo, F., 2006: Heat and freshwater transport through the central Labrador Sea. *J. Phys. Oceanogr.*, **36**, 606–628, doi:10.1175/JPO2875.1.

Talley, L. D., and M. S. McCartney, 1982: Distribution and circulation of Labrador Sea Water. *J. Phys. Oceanogr.*, **12**, 1189–1205, doi:10.1175/1520-0485(1982)012<1189:DACOLS>2.0.CO;2.

van Aken, H. M., M. F. de Jong, and I. Yashayaev, 2011: Decadal and multi-decadal variability of Labrador Sea Water in the north-western North Atlantic Ocean derived from tracer distributions: Heat budget, ventilation, and advection. *Deep-Sea Res. I*, **58**, 505–523, doi:10.1016/j.dsr.2011.02.008.

Vellinga, M., and R. A. Wood, 2002: Global climatic impacts of a collapse of the Atlantic thermohaline circulation. *Climatic Change*, **54**, 251–267, doi:10.1023/A:1016168827653.

Wolfe, C. L., and C. Cenedese, 2006: Laboratory experiments on eddy generation by a buoyant coastal current flowing over variable bathymetry. *J. Phys. Oceanogr.*, **36**, 395–411, doi:10.1175/JPO2857.1.

Yashayaev, I., 2007: Hydrographic changes in the Labrador Sea, 1960–2005. *Prog. Oceanogr.*, **73**, 242–276, doi:10.1016/j.pocean.2007.04.015.

Zhang, W., and X.-H. Yan, 2014: Lateral heat exchange after the Labrador Sea deep convection. *J. Phys. Oceanogr.*, **44**, 2991–3007, doi:10.1175/JPO-D-13-0198.1.